Effect of alumina additions on the anode|electrolyte interface in solid oxide fuel cells

R. Knibbe [a], J. Drennan [a,*], A. Dicks [a], J. Love [b]

[a] *Centre for Microscopy and Microanalysis, The University of Queensland, St Lucia Queensland 4072, Australia*
[b] *Ceramic Fuel Cells Limited, 170 Browns Road, Noble Park, Victoria 3174, Australia*

Abstract

The longevity of a solid oxide fuel cell (SOFC) stack is curtailed by the fragility of its ceramic components. At Ceramic Fuel Cells Limited (CFCL), 15 wt.% alumina is added to the commonly used 10 mol% Y_2O_3–ZrO_2 (YSZ) electrolyte to improve both the fracture toughness and grain-boundary conductivity of the electrolyte. This study investigates the effect of such addition of alumina on the anode|electrolyte interface; more specifically, which reactions occur with the Al_2O_3 at the interface and how these reactions influence fuel cell performance. X-ray diffraction (XRD), scanning electron microscopy (SEM) and transmission electron microscopy (TEM) are used to characterize the formation of $NiAl_2O_4$ in the alumina regions in the electrolyte. The $NiAl_2O_4$ is observed to grow into the adjacent grain boundaries to form an interconnected $NiAl_2O_4$ network up to 4 μm deep into the electrolyte. Impedance spectroscopy shows that the formation of $NiAl_2O_4$ does not affect the grain bulk ionic conductivity. The grain-boundary conductivity is markedly reduced at low temperatures. However, at the high SOFC operating temperature at CFCL (850 °C) the contribution of the grain-boundary conductivity to the total conductivity is diminished, and the $NiAl_2O_4$ is found not to have an effect on the total electrolyte conductivity and is deemed not to be a detrimental reaction.
Crown Copyright © 2008 Published by Elsevier B.V. All rights reserved.

Keywords: Solid oxide fuel cell; Nickel aluminate; Interface; Yttria-stabilized zirconia; Ionic conductivity; Transmission electron microscopy

1. Introduction

The high operating temperature (typically 750–1000 °C) of electrolyte-supported solid oxide fuel cells (SOFCs) is dictated by the oxide ion conductivity of the electrolyte. Beneficially, the high operating temperature increases the electrode kinetics and also allows for internal reforming of hydrocarbon fuels. On the other hand, the high manufacturing and operating temperatures that are demanded by ceramic fuel cell materials promote material interaction and degradation, and thus limit the material choices. Furthermore, the thermal stresses induced by the high operating temperatures encourage interfacial stress and delamination of contiguous fuel cell components.

Despite extensive investigations into alternative electrolytes, yttria-stabilized zirconia (YSZ) still remains the most popular electrolyte material due to its stability, strength and low cost. In

an attempt to reduce the sintering temperature of cubic zirconia, Radford and Bratton [1,2] added various oxides, including alumina, to YSZ. Although alumina only decreased the sintering temperature of YSZ by ∼100 °C, it was found that such an addition improved the YSZ grain-boundary conductivity [3,4]. This discovery resulted in a plethora of studies on the effect of alumina additions on the conductivity of zirconia [5–12].

It is argued that alumina acts as a 'getter' of the silicon impurities, which are ubiquitous in zirconia from processing [11]. The mechanism suggests that the siliceous grain-boundary phase preferentially associates with the alumina grains—ultimately 'cleaning' the YSZ grain boundaries. This increases the grain-to-grain connectivity and results in an increased grain-boundary conductivity. The main trade-off with alumina is that it decreases the bulk conductivity of the electrolyte as it is an ionic insulator and exists as a second phase.

The other major benefit of alumina additions is that alumina increases the fracture toughness and Young's modulus of YSZ and therefore decreases the probability of fracture. Tekeli [12] reported an increase in fracture toughness from

1.5 to 2.41 MPa $\sqrt{m}$ when 10 wt.% Al_2O_3 was added to 8YSZ (16 mol% Y_2O_3 ZrO_2). At Ceramic Fuel Cells Limited (CFCL), 15 wt.% Al_2O_3 is added to a 10YSZ (20 mol% Y_2O_3–ZrO_2) electrolyte to improve both the grain-boundary conductivity and strength.

The present study looks at the reaction between the anode and the electrolyte during fuel cell synthesis and at the subsequent anode reduction and fuel cell operation. The work was stimulated by observations at CFCL that an uncharacteristic blue phase was forming on the surface of the typically white electrolyte during anode sintering. As nickel aluminate ($NiAl_2O_4$) is known to form a bright blue phase when NiO is reacted with Al_2O_3, it was therefore anticipated that this blue phase was indeed $NiAl_2O_4$. Nickel aluminate has been shown to reduce to nickel and alumina in a sufficiently reducing atmosphere [13], therefore the stability of the nickel aluminate during anode reduction and fuel cell operation is of interest. In addition, the location and morphology of the nickel aluminate is of great importance as $NiAl_2O_4$ has a very low oxygen diffusivity [14] and would severely inhibit the oxide ion conductivity of the electrolyte if an interconnected layer was to form.

During both anode reduction and fuel cell operation, the $NiAl_2O_4$ would experience a reducing atmosphere. Various authors have reported the partial reduction of $NiAl_2O_4$ to Ni and Al_2O_3 and that this is accompanied by an 18% volume decrease [15,16]. The $NiAl_2O_4$ cannot easily accommodate such a volume reduction and therefore microcracks form at the interface between the unreduced and reduced spinel [16]. The formation of microcracks in the $NiAl_2O_4$ would be detrimental as the structural integrity of YSZ would be reduced. After anode reduction, when all of the NiO has reduced to Ni, the formation of $NiAl_2O_4$ is no longer feasible.

The anode oxygen partial pressure $P_{O_2\text{-anode}}$ would be the lowest during anode reduction, i.e., when the cells were at an open-circuit voltage (OCV). For an anode environment of 60% H_2/40% H_2O at 850 °C, the $P_{O_2\text{-anode}}$ is calculated to be 3.6×10^{-13} Pa. From the NiO–Al_2O_3 thermodynamic stability diagram, the spinel ($NiAl_2O_4$) stability limit is 4.9×10^{-9} Pa at 940 °C [13], but the lower operating temperature (850 °C) of the fuel cell would therefore require a lower oxygen partial pressure to reduce the $NiAl_2O_4$. As the calculated values of $P_{O_2\text{-anode}}$ during anode reduction are significantly lower than the spinel stability limit, $NiAl_2O_4$ reduction is anticipated.

Investigations have been conducted on the anode|electrolyte interface with YSZ as the electrolyte (Linderoth et al. [17] and Liu and Jiao [18]), but to date no work has been reported on the effect of alumina additions to the electrolyte on the interface.

The aim of the present research is to examine the anode|electrolyte interfaces after fuel cell production, anode reduction and prolonged fuel cell operation using X-ray diffraction (XRD), scanning electron microscopy (SEM) and transmission electron microscopy (TEM). Subsequently, the influence of anode|electrolyte interactions on the electrical performance is investigated using impedance spectroscopy. This study is performed on samples based on the electrolyte-

supported fuel cell design employed by CFCL. The electrolyte is a composite of 15 wt.% Al_2O_3 in 10YSZ; the anode is the typical Ni-YSZ cermet manufactured from NiO and YSZ.

2. Experimental methods

2.1. Material synthesis

The following fuel cell manufacturing process is used at CFCL. 15 wt.% Al_2O_3 (Alcoa) is mechanically mixed with 10YSZ (Mel Chemicals). The mixture is tape cast, dried and laser cut into the desired circular shape with a diameter of 13.2 cm. The electrolyte is fired at 1600 °C for 1 h. Once the electrolyte is fired, an 8-cm diameter concentric, 10 μm thick circular functional anode layer is printed on to the electrolyte surface. The anode consists of a 50:50 mixture of NiO and 10YSZ. The second layer (overlayer) contains CeO_2 and is printed on to the functional anode layer. The two anode layers and the gas-diffusion layer (GDL) are co-fired at 1300 °C for 6 h. To complete fuel cell production, the cathode and GDL layer are fired at 1150 °C for 2 h.

2.2. Physical material characterization

Three different types of samples were examined for materials characterization—after fuel cell production (unreduced), after anode reduction (reduced) and after 500 h of fuel cell operation (operated). The anode sample was reduced at 850 °C in a flowing (65 ml H_2 min^{-1}) atmosphere for 2 h and fuel cell operation was carried out at 850 °C in a 60% H_2/40% H_2O flowing atmosphere for 500 h. Physical materials characterization was performed using XRD, SEM and TEM.

2.2.1. X-ray diffraction (XRD)

To analyze interfacial reactions at the anode|electrolyte interface, the samples were prepared by grinding off the bulk of the anode layers using SiC paper. X-ray diffraction was performed on the remaining solid electrolyte which also contained the anode|electrolyte interface and some of the remnant anode. The analysis was performed with a Bruker D8 Advance X-ray diffractometer with parallel beam geometry and a graphite monochromator using Cu Kα radiation. Measurements were carried out from $2\theta = 2°$ to 90° using a step size of 0.02° at a speed of 1° per minute. Compounds were identified using peak search Diffrac Plus V 9.0 software.

2.2.2. Scanning electron microscopy (SEM)

The samples were mounted in epoxy resin and were vacuum embedded. The samples were ground using SiC paper, polished using 6, 3 and 1 μm diamond paste, and then carbon-coated to eliminate surface charging.

The morphology of the samples was observed with a JEOL6460 LA SEM equipped with a tungsten filament and JEOL JED 2300 Energy Dispersive X-ray Spectrometry (EDS) detector in secondary and backscattered electron (BSE) mode using an accelerating voltage of 15 keV. X-ray mapping was

performed using the aforementioned SEM in conjunction with JEOL Analysis Station Software.

2.3. Transmission electron microscopy (TEM)

The samples were prepared for TEM investigations using the tripod polishing method and a focused ion beam (FIB). For the tripod samples, 4 mm × 5 mm sections were cut from the samples using a Gatan ultrasonic rectangular cutter. Four sections were thinly coated with an epoxy resin and placed in a Teflon mould. The stack was cured for 30 min at 120 °C. Once cured, the stack was cut into 1.5 mm slices by means of a Struers Accutom 50 fitted with a diamond cut-off wheel. Using a tripod polisher, a wedge sample was made using 30, 15, 6, 3, 1, 0.5 and 0.1 μm diamond film. The samples were then thinned to electron transparency with a Gatan Precision Ion Polishing System (PIPS).

Samples of the unreduced and the reduced anode|electrolyte interface were examined with an XT Nova Nanolab 200 dual beam FIB, operated with a 30-keV Ga$^+$ ion beam.

Samples were investigated with a Phillips Technai F20 scanning transmission electron microscope (STEM). The F20 was operated at 200 keV and was equipped with a field emission zirconia-coated tungsten filament and an EDAX Ltd. thin-window EDS detector.

2.4. Impedance spectroscopy

Two types of samples were investigated using impedance spectroscopy, namely, a 15-wt.% Al_2O_3-YSZ electrolyte (15A10YSZ) and a NiO reacted 15A10YSZ sample (15A10YSZ $NiAl_2O_4$).

A set of 15A10YSZ samples were reacted with NiO to form $NiAl_2O_4$ on the electrolyte surface. The sintering technique and profile used were employed to mimic the sintering of the anode on to the electrolyte during typical fuel cell production at CFCL. The major difference is that the $NiAl_2O_4$ reaction is occurring on both sides of the electrolyte to create a ~8-μm thick reaction layer in total. The electrolyte samples were placed in a bed of NiO in a platinum crucible with a lid to prevent possible furnace contamination of the sample. The samples were fired at 1300 °C for 6 h with a heating and cooling ramp rate of 3 °C per min. After firing, the samples were placed in a beaker with dilute HCl and slightly heated to remove any excess NiO.

Platinum electrodes were painted on to the samples using No. 6082 Englehard platinum paste and then fired in air at 850 °C for 1 h with a heating and cooling rate of 3 °C per min. Two-terminal a.c. impedance measurements were carried out in air from 230 to 800 °C using a Solartron 1260 impedance analyser operated with a 100-mV root mean square (RMS) amplitude and ZPlot/View software. At temperatures below 230 °C, the impedance of the sample exceeds 1 MΩ, which is beyond the probing capabilities of the Solartron 1260 Impedance Analyser.

The data was geometry corrected by using a *A*/*l* multiplier in the Nyquist plots, where *A* is the surface area of the sample and *l* is the sample thickness. To determine the bulk, grain-boundary and total conductivity, the Nyquist plots were fitted using an equivalent circuit model of a resistor in series with two RC couples.

3. Results

3.1. X-ray diffraction

Representative XRD scans are shown in Fig. 1. Cubic YSZ phase is seen in all of the scans as it is the main component of the electrolyte and a significant component of the anode. Similarly, weak Al_2O_3 peaks (from the electrolyte) are observed in all of the XRD scans.

Strong NiO peaks (from the anode) are found in the unreduced sample. These NiO peaks are fully replaced by Ni peaks in the reduced and operated samples, showing a reduction of NiO to Ni. As cubic NiO has a lattice parameter of 4.177 Å and cubic Ni has a lattice parameter 3.524 Å, the Ni peaks are shifted to higher 2θ relative to the NiO peaks. The stronger intensity of the Ni peaks indicates a higher nickel content in the operated sample, which is merely due to less anode bulk being removed during XRD sample preparation, which was difficult to control.

Several additional peaks are observed in the unreduced XRD pattern at ~31.7°, 45.5° and 68.8° and these peaks are attributed to $NiAl_2O_4$. The other major $NiAl_2O_4$ peaks are overlapped by the NiO and YSZ peaks, which dominate due to their higher concentrations. The most significant is the strongest $NiAl_2O_4$ peak of the {1 1 3} planes, which is overlapped by the NiO {1 1 1} peak at ~37.8°.

The reduction of NiO to Ni allows the strongest $NiAl_2O_4$ {1 1 3} peak to be seen at ~37° in the reduced and operated samples. The presence of the $NiAl_2O_4$ peaks indicates that after anode reduction the $NiAl_2O_4$ phase is not fully reduced. The reduction of $NiAl_2O_4$ would form Ni and alumina, as these are both already present in the sample, X-ray diffraction analysis provides no information on the partial reduction of $NiAl_2O_4$.
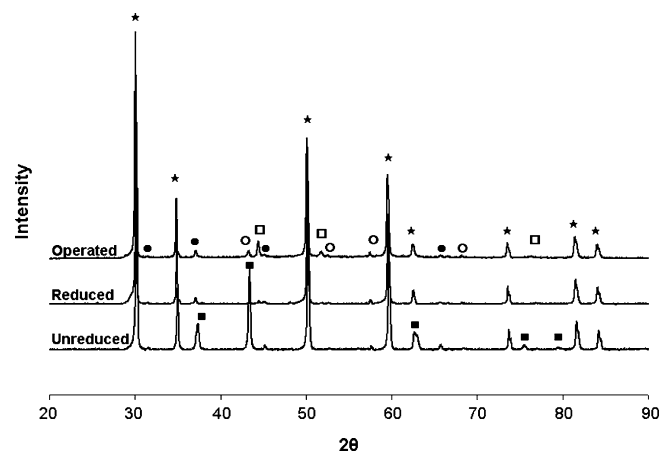

Fig. 1. XRD scans of unreduced, reduced and operated anode|electrolyte samples. YSZ: *; NiO: ■; Ni: □; Al_2O_3: ○; $NiAl_2O_4$: ●.
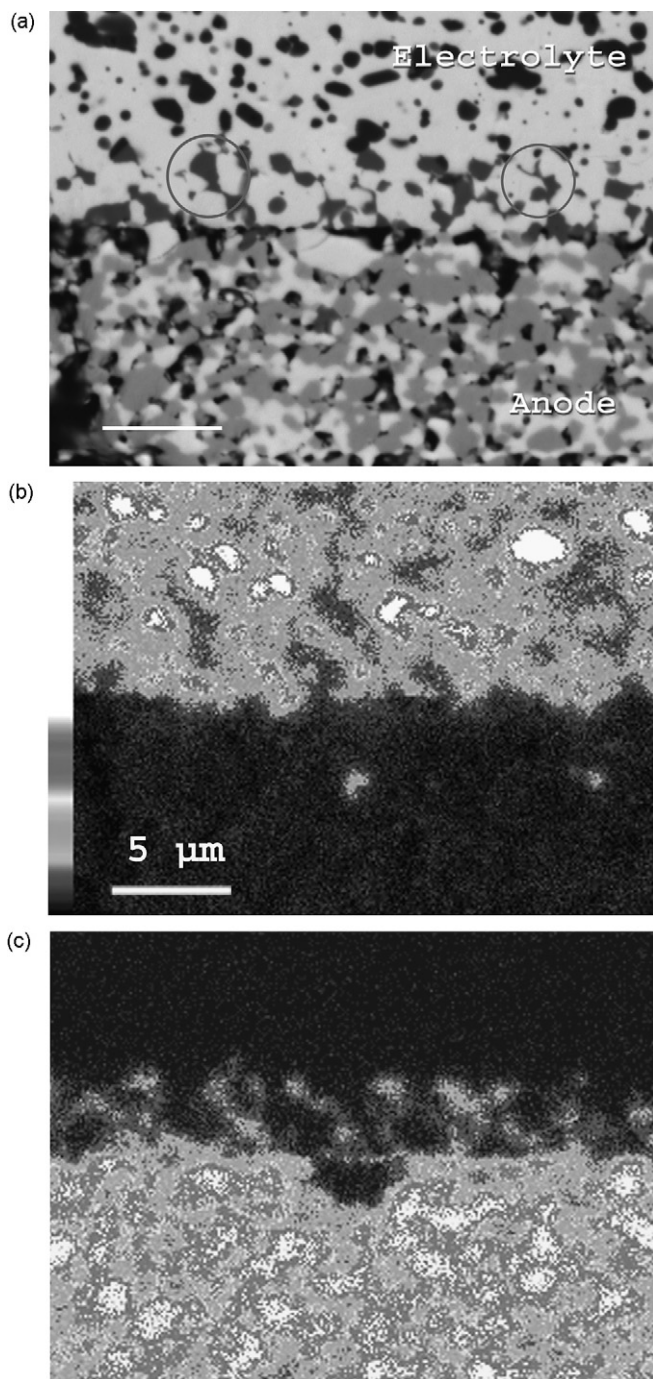
Fig. 2. SEM backscattered micrograph of typical anode|electrolyte interface after anode sintering, with corresponding Al (b) and Ni (c) elemental maps. Ni map shows migration of nickel from anode region into electrolyte grain boundaries and alumina grains. Circled areas are $NiAl_2O_4$ grains.

3.2. Electron microscopy

3.2.1. Unreduced sample

Fig. 2(a) shows a backscattered electron (BSE) image of the unreduced fuel cell interface. The difference in grey scale in the image reflects a chemical composition difference—the dark grains have a lower average atomic number, whereas the light grains have a higher average atomic number. The average atomic number of Al_2O_3, YSZ and NiO is 10.0, 18.7 and 18.0, respectively. Therefore, the Al_2O_3 grains appear the darkest and the YSZ grain the lightest. The small difference in average atomic number, between NiO and YSZ results in only a slight difference in grey scale contrast between the NiO grains and YSZ grains in the anode. The darkest regions in the anode are open pores filled with epoxy with a low atomic number of 6.

At the interface, there is a light grey phase which is seen to grow ~4 μm into the electrolyte region and has replaced the dark alumina grains. Elemental maps (Fig. 2(b) and (c)) show that this area is rich in both aluminium and nickel. This suggests that $NiAl_2O_4$ formation as expected from XRD phase analysis. $NiAl_2O_4$ has an average atomic number of ~12.3 and should appear darker than alumina, but lighter than both YSZ and NiO, which is consistent with the grey scale contrast observed.

TEM selected area diffraction (SAD) (Fig. 3) provides further irrefutable evidence that the grains forming in the electrolyte are $NiAl_2O_4$.

On closer inspection of the SEM nickel map (Fig. 2(c)), it is observed that the nickel is not only present in the alumina grains, but also in the surrounding grain boundaries. There are two reasons for the presence of the nickel in the grain boundaries of the electrolyte, namely: (i) the formation of $NiAl_2O_4$ is associated with a 7% volume expansion of the original NiO and Al_2O_3; (ii) the grain boundaries provide a fast diffusion path for the nickel to the alumina grains.

Further evidence for the expansion of the $NiAl_2O_4$ can be obtained when comparing the spherical morphology of the Al_2O_3 grains deep in the electrolyte with the $NiAl_2O_4$ grains at the anode|electrolyte interface, which are invariably associated with thin regions that taper off into the adjoining grain boundaries (circled areas in Fig. 2(a)).

As the nickel diffusion through the alumina and the grain boundaries produce a very even migration front, it is postulated that NiO is supplied to the electrolyte in both a solid and vapour form. Several authors, including de Roos et al. [19], have reported NiO vapourisation starting at 1100 °C.
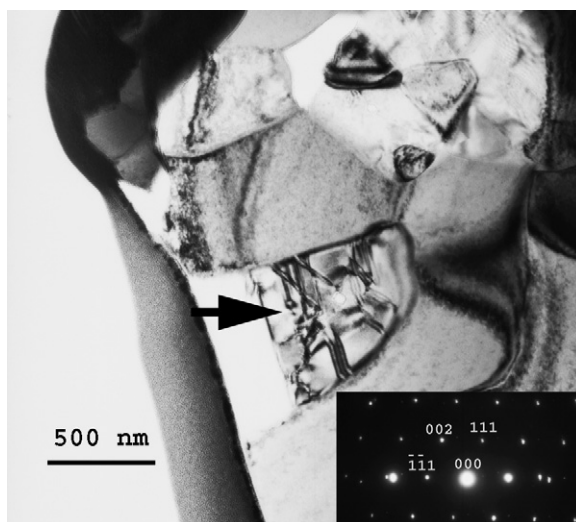

Fig. 3. TEM micrograph of $NiAl_2O_4$ grain (marked with arrow) prior to anode reduction, with ⟨0 1 1⟩ selected area diffraction inset.

The presence of the nickel in the electrolyte grain boundaries in the form of both diffusing nickel and expanded $NiAl_2O_4$ is of major significance to the ionic conductivity of the electrolyte. YSZ grain boundaries pose a significant barrier to the migration of oxide ions during the operation of fuel cells. In the current study, the electrolyte grain boundaries are significantly contaminated with nickel to a depth of 4 μm.

3.3. Reduced sample

After anode reduction, $NiAl_2O_4$ is still observed at the anode|electrolyte interface and the $NiAl_2O_4$ microstructure at the interface is unaltered. Nickel and aluminium elemental maps (Fig. 4) of the FIB TEM sample clearly show the presence of nickel in the alumina grains in the electrolyte. The micrograph also shows grains that have clearly grown out into the adjacent grain boundaries, i.e., similar to what is seen in Figs. 2 and 3.

A typical $NiAl_2O_4$ grain taken in dark-field mode using TEM SAD is shown in Fig. 5. The micrograph highlights the 'squeezed' morphology of the grain. The additional reflections observed in the SAD are from an adjacent YSZ grain. The partial reduction of $NiAl_2O_4$ would result in the presence of additional reflections in the SAD pattern from either alumina or nickel, or microcracks between the reduced and unreduced $NiAl_2O_4$ should be observed in the micrographs. As none of these are found in the $NiAl_2O_4$ at the anode|electrolyte interface, it is concluded that the $NiAl_2O_4$ is neither fully nor partially reduced during anode reduction.

3.4. Operated sample

Even after 500 h of fuel cell operation, $NiAl_2O_4$ is still found (Fig. 6(a)) within the first several microns of the electrolyte. The aluminium and nickel elemental maps (Fig. 6(b) and (c)) appear similar to those observed for both the unreduced and reduced samples. Furthermore, the lack of additional reflections in the TEM SAD pattern (Fig. 7) and the homogeneity of the $NiAl_2O_4$ grain confirms that the $NiAl_2O_4$ is still stable after 500 h of fuel cell operation.

Full or partial reduction of $NiAl_2O_4$ is expected as the oxygen partial pressure of 3.6×10^{-13} Pa is significantly lower than the previously reported spinel stability limit of 4.9×10^{-9} Pa at 940 °C. The lack of $NiAl_2O_4$ reduction could be due to a number of factors such as: (i) the oxygen partial pressure calculated is the most severe and would only occur at the fuel inlet during OCV and therefore the actual oxygen partial pressure at the anode|electrolyte interface would be much higher; (ii) 850 °C is an insufficient temperature to initiate the $NiAl_2O_4$ reduction; (iii) the oxygen supply from the electrolyte could increase the oxygen activity and stave off $NiAl_2O_4$ reduction.

Due to the stability and interconnected nature of the $NiAl_2O_4$ phase in the electrolyte, it is of paramount importance to understand the effect that $NiAl_2O_4$ has on fuel cell performance. From a mechanical standpoint, the stability of the interface is of interest as the formation of microcracks would impair the mechanical integrity.
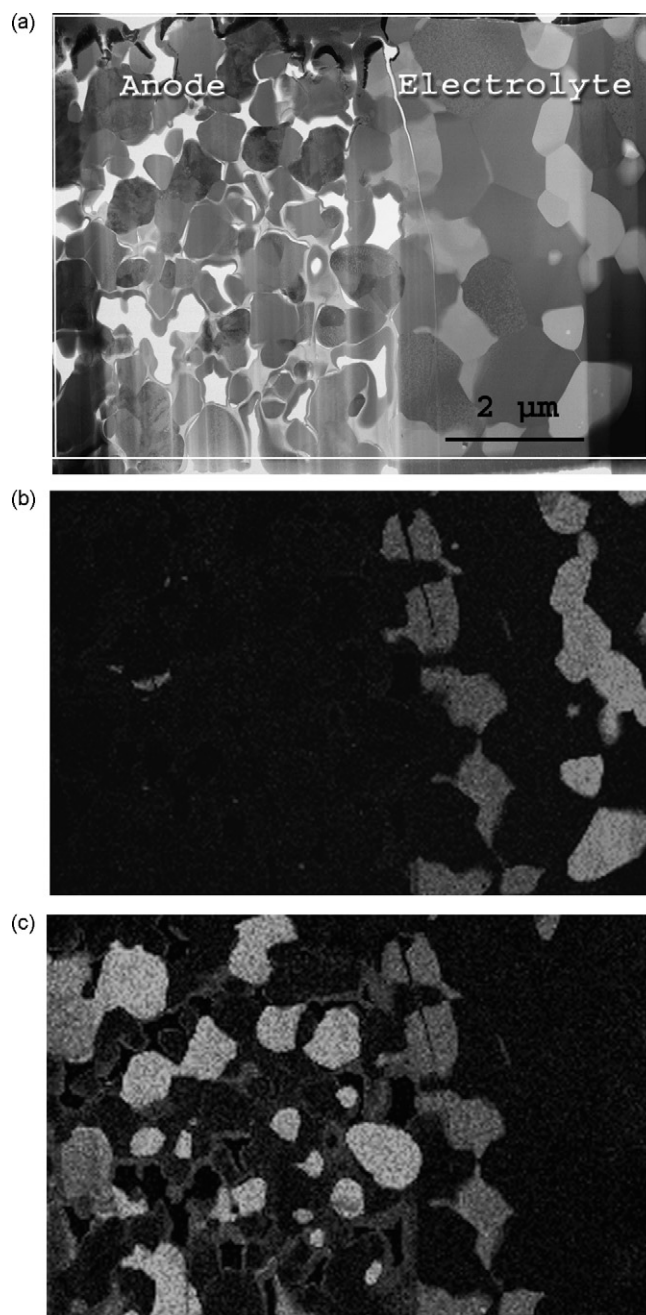

Fig. 4. STEM micrograph of anode|electrolyte interface after anode reduction, with corresponding Al (b) and Ni (c) elemental maps. From nickel elemental map, nickel aluminate is still found in electrolyte and appears unaltered after anode reduction.

3.5. Impedance spectroscopy

In order to evaluate the effect of $NiAl_2O_4$ formation on the ionic conductivity of the 15A10YSZ electrolyte, a.c. impedance spectroscopy was performed on two sets of samples, namely, unreacted 15A10YSZ samples and reacted 15A10YSZ samples (15A10YSZ/$NiAl_2O_4$).

A series of Nyquist plots for four temperatures, 378, 400, 423 and 449 °C, is given in Fig. 8. The first arc represents the grain bulk impedance and the second arc represents the grain-
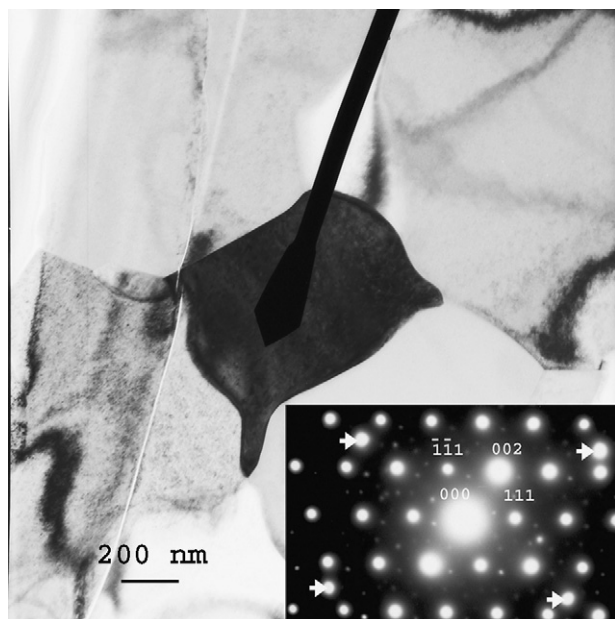
Fig. 5. Dark-field TEM micrograph of NiAl$_2$O$_4$ grain after anode reduction, in YSZ matrix with $\langle 0\,1\,1 \rangle$ selected area diffraction pattern inset. Additional reflections in pattern, indicated by arrows, are attributed to YSZ from adjacent grain. NiAl$_2$O$_4$ grows out into surrounding grain boundaries.

boundary impedance, followed by an electrochemical response. The frequency of the point at the maxima of each arc is referred to as the point of equivalence ω_0. The shape of the curve remains unaltered at the various temperatures, but as the temperature increases the resistance of the electrolyte samples decreases. The lower resistance at higher temperatures consequently decreases the relaxation time (τ) and increases the point of equivalence (ω_0) in accordance with

$$\tau = \frac{1}{\omega_0} = RC \qquad (1)$$

where R is the resistance, C is the capacitance, τ is the relaxation time (or time constant), and ω_0 is the angular frequency at the point of equivalence.

At sufficiently high temperatures, the point of equivalence is shifted to frequencies higher than the maximum 1 MHz probing frequency of the Solartron 1260. Consequently, the detail in the Nyquist plots is lost and, as fewer data points are being modelled, inaccuracies are introduced in curve fitting. At 378 °C (Fig. 8), most of the bulk and grain-boundary impedance curves can be seen, but as the temperature increases to 449 °C, the equivalence point of the bulk is at too high a frequency to be measured and hence modelled, and only the full grain-boundary impedance response is seen.

Fig. 9 shows Nyquist plots for 15A10YSZ and 15A10YSZ NiAl$_2$O$_4$ taken at 378 °C. The bulk conductivity (σ_{bulk}) does not vary within experimental error between the two samples with σ_{bulk} calculated as $2.36 \pm 0.06 \times 10^{-5}$ and $2.39 \pm 0.06 \times 10^{-5}$ S cm^{-1} for 15A10YSZ and 15A10YSZ NiAl$_2$O$_4$, respectively. The grain-boundary conductivity (σ_{gb}) is $\sim$26% higher in the unreacted 15A10YSZ sample with σ_{gb} cal-
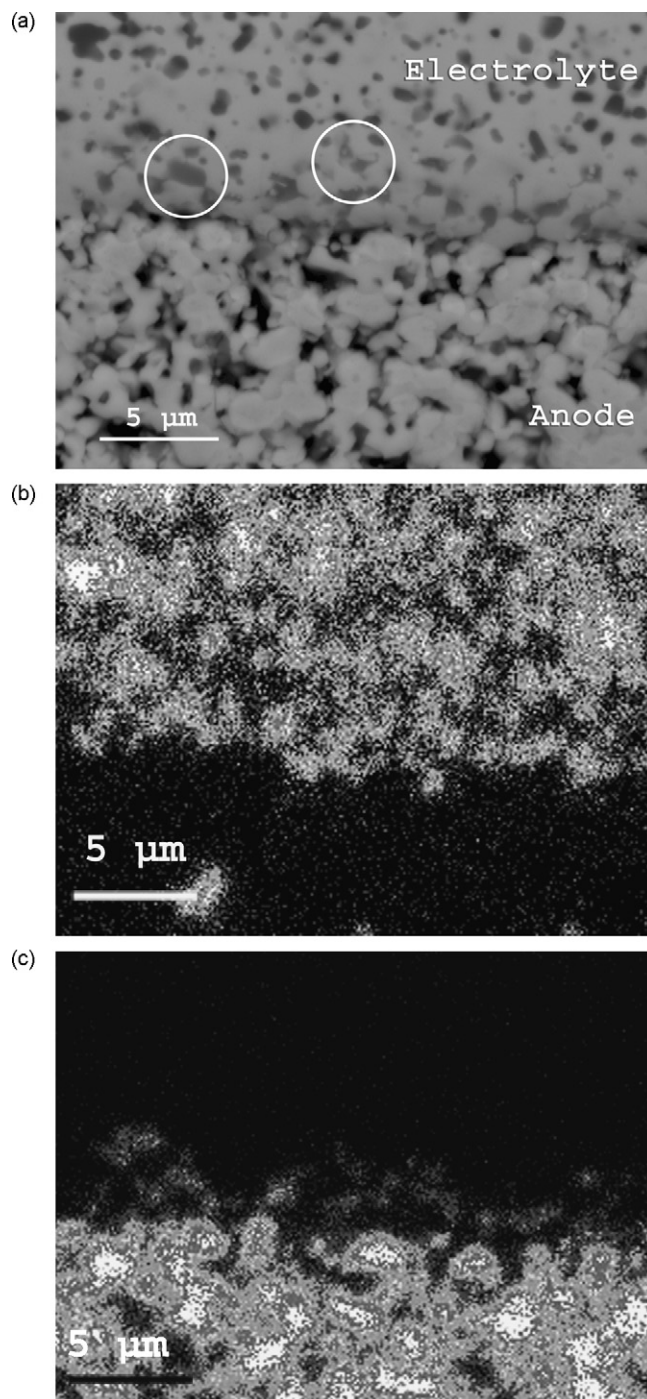

Fig. 6. SEM micrographs of anode electrolyte interface after 500 h of fuel cell operation, with corresponding Al (b) and nickel (c) maps. Maps still show presence of nickel in electrolyte grain boundaries and alumina grains.

culated as $2.32 \pm 0.06 \times 10^{-5}$ and $2.91 \pm 0.07 \times 10^{-5}$ S cm^{-1} for 15A10YSZ and 15A10YSZ NiAl$_2$O$_4$, respectively. Similar trends are observed at all temperatures.

The best way to present this data is by fitting the model and plotting the Arrhenius relationship

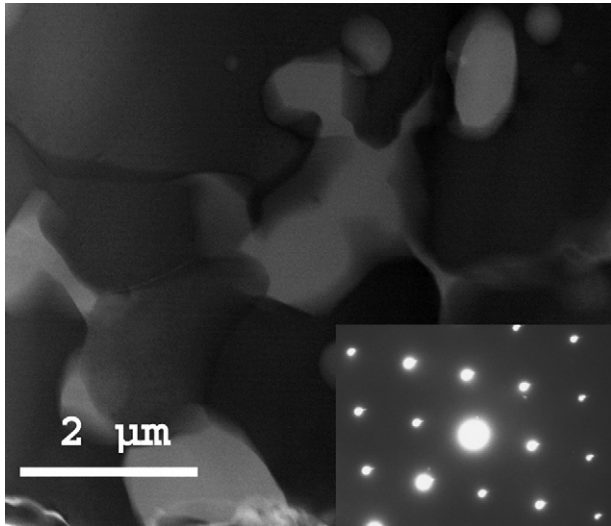$$\sigma T = A_\sigma \exp\left(\frac{-E_\sigma}{kT}\right)$$

Fig. 7. STEM images of anode|electrolyte interface after 500 h of fuel cell operation, with $\langle 0\,1\,1 \rangle$ selected area diffraction pattern inset.
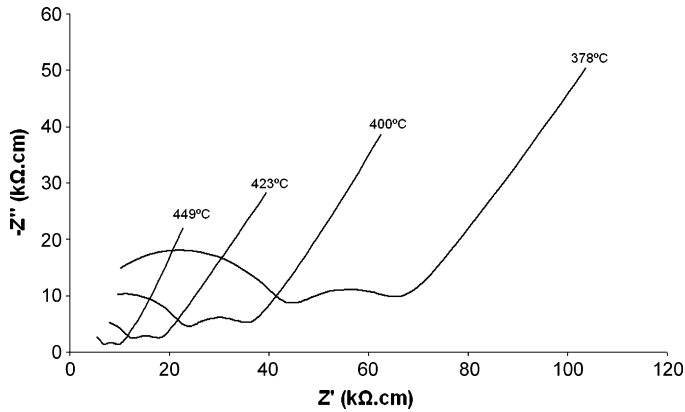

Fig. 8. Nyquist plots of 15A10YSZ electrolyte at various temperatures, geometry and density corrected. At higher temperatures, point of equivalence exceeds maximum probing frequency of Solartron 1260 and therefore bulk impedance is lost.
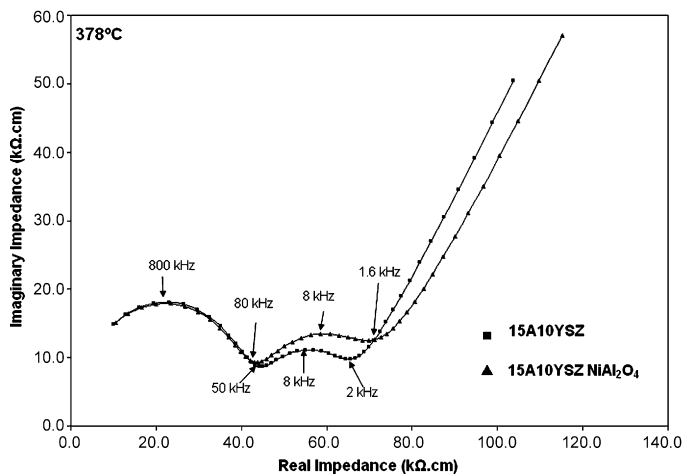

Fig. 9. Nyquist plots of 15A10YSZ and 15A10YSZ $NiAl_2O_4$ at 378 °C. High-frequency grain bulk impedance appears identical between two samples, but low-frequency grain-boundary impedance is markedly higher in 15A10YSZ $NiAl_2O_4$.
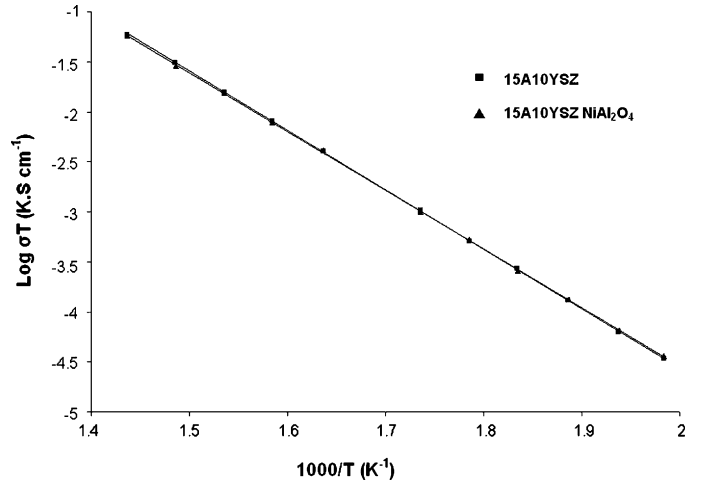

Fig. 10. Arrhenius plot of bulk conductivity of 15A10YSZ and 15A10YSZ $NiAl_2O_4$ samples.

where σ is the conductivity, T is the temperature, A_σ is the pre-exponential constant, and E_σ is the activation energy for conduction.

The Arrhenius plot of the bulk conductivity (Fig. 10) shows that the $NiAl_2O_4$ reaction has no effect on the bulk conductivity of the 15A10YSZ electrolyte. Additionally, any nickel diffusion through the YSZ grains in the 15A10YSZ/$NiAl_2O_4$ sample has a negligible effect on the bulk conductivity. The grain bulk activation energies of 15A10YSZ and 15A10YSZ/$NiAl_2O_4$ are 1.16 ± 0.03 and 1.17 ± 0.03 eV, respectively, which are similar to the activation energies reported by Feighery et al. [5]. The activation energy of 15A10YSZ/$NiAl_2O_4$ is only 1% higher than that of 15A10YSZ, and is within experimental error. This finding indicates a similar transport mechanism in the grain bulk of the two samples.

A significant decrease in the grain-boundary conductivity (Fig. 11) is observed in the reacted 15A10YSZ/$NiAl_2O_4$ sample. At 231 °C, the conductivity of the 15A10YSZ grain-boundary ($7.76 \pm 0.19 \times 10^{-8}$ S cm^{-1}) is 38% higher than that of the 15A10YSZ/$NiAl_2O_4$ ($5.61 \pm 0.14 \times 10^{-8}$ S cm^{-1}). The large
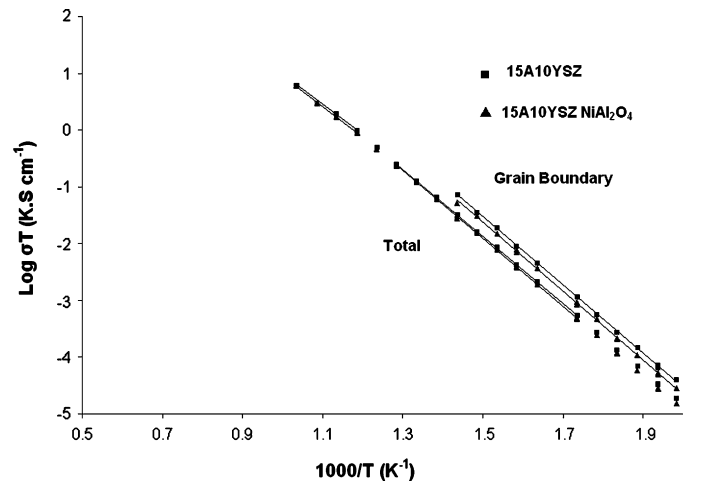

Fig. 11. Arrhenius plot of grain-boundary and total conductivity of 15A10YSZ and 15A10YSZ $NiAl_2O_4$.

Table 1
A_σ and E_σ for 15A10YSZ and 15A10YSZ/NiAl$_2$O$_4$ in low-temperature (300–500 °C) and high-temperature (600–800 °C) regions

	Low temperature (300–500 °C)			High temperature (600–800 °C)	
	A_σ	E_σ (eV)		A_σ	E_σ (eV)
15A10YSZ	9.88×10^6	1.17		1.62×10^6	1.04
15A10YSZ/NiAl$_2$O$_4$	10.99×10^6	1.18		2.16×10^6	1.07

difference in grain-boundary conductivities indicates that the diffusion of the nickel into the YSZ grain boundaries and the growth of the NiAl$_2$O$_4$ into the grain boundaries impede the conduction of oxide ions through the grain boundaries. At 400 °C, the grain-boundary conductivity is still 16% lower in the reacted 15A10YSZ/NiAl$_2$O$_4$ sample than in the unreacted sample.

The grain-boundary activation energies of the 15A10YSZ and 15A10YSZ/NiAl$_2$O$_4$ samples are 1.19 ± 0.03 and 1.20 ± 0.03 eV, respectively, which are similar to the grain-boundary activation energies reported by Rizea et al. [9]. The activation energies of 15A10YSZ and 15A10YSZ/NiAl$_2$O$_4$ are the same within experimental error. This suggests a similar transport mechanism in the grain boundaries of the two samples.

Although there is a significant difference in the grain-boundary conductivity at low temperatures, the total conductivity of the electrolyte is of higher importance to fuel cell performance (Fig. 11). The Arrhenius plot of the total conductivity shows that at 231 °C the conductivity of the 15A10YSZ/NiAl$_2$O$_4$ sample ($3.06 \pm 0.08 \times 10^{-8}$ S cm^{-1}) is ~22% lower than that of the unreacted 15A10YSZ sample ($3.74 \pm 0.09 \times 10^{-8}$ S cm^{-1}). When the temperature is increased, the conductivities begin to converge and at 570 °C the conductivity of the 15A10YSZ/NiAl$_2$O$_4$ sample is only 6% lower than that of the 15A10YSZ sample. At 700 °C, there is no difference in the total conductivities.

Previous authors [9,20,21] have reported that the bulk activation energy of YSZ is characterised by two regions, viz., a low-temperature (300–500 °C) and a high-temperature (600–800 °C) region. At high temperature, the bulk activation energy decreases, but the grain-boundary activation energy remains unaffected. From the Arrhenius plot of the total conductivity (Fig. 11), A_σ and E_σ were determined for the abovementioned two regions; the results are given in Table 1.

The total conductivity at 850 °C of the 15A10YSZ sample is 0.0310 ± 0.001 S cm^{-1}, which is the same as the conductivity for 15A10YSZ/NiAl$_2$O$_4$. This is consistent with previous in-house tests at CFCL, in which the conductivity of the 15A10YSZ electrolyte was measured to be 0.033 S cm^{-1} at 850 °C [22].

The trend indicates that at the high temperatures of fuel cell operation, the NiAl$_2$O$_4$ has little effect on the total conductivity of the electrolyte. Due to the higher activation of the grain boundaries, at high temperatures the grain-boundary conductivity increases faster than the bulk conductivity, which has a lower activation energy at high temperature (≥600 °C) [9,20,21]. Therefore, at high operating temperatures, the grain-boundary contribution to the total resistivity diminishes.

4. Conclusions

This study sought to examine the effect of alumina additions to the YSZ electrolyte on the anode|electrolyte interface in SOFCs at CFCL. From investigations with XRD, SEM, TEM and impedance spectroscopy, the following conclusions are drawn.

- During anode sintering on to the YSZ-Al$_2$O$_3$ electrolyte, NiAl$_2$O$_4$ forms in the electrolyte and replaces the alumina grains up to a depth of 4 μm.
- The NiAl$_2$O$_4$ tapered morphology is created by the 7% expansion required to accommodate the reaction and this forces the NiAl$_2$O$_4$ reactant into the grain boundaries.
- Grain boundaries up to a depth of 4 μm into the electrolyte are also filled with diffusing Ni.
- No signs of NiAl$_2$O$_4$ reduction, in the form of microcracks or additional reflections in the TEM SAD, are found in the reduced or operated fuel cells. Due to the stability of NiAl$_2$O$_4$, it is not considered detrimental to the mechanical integrity of the interface.
- NiAl$_2$O$_4$ formation decreases the conductivity of the grain boundaries in the electrolyte, but does not affect the bulk/grain conductivity. At low temperatures, therefore, the total conductivity is impeded by the formation of NiAl$_2$O$_4$ but at the present SOFC operating temperature of 850 °C NiAl$_2$O$_4$ does not affect the total conductivity of the electrolyte and is therefore concluded not to be of detrimental to the performance of the fuel cell.

The addition of alumina is an effective way to increase the fracture toughness of the YSZ electrolyte. Despite the formation of NiAl$_2$O$_4$, this does not have an adverse effect on the conductivity of the electrolyte. If the operating temperature of the SOFC was to be lowered, however, this study indicates that the NiAl$_2$O$_4$ would begin to impede the oxide ion conductivity of the electrolyte.

References

[1] K.C. Radford, R.J. Bratton, J. Mater. Sci. 14 (1979) 59–65.
[2] K.C. Radford, R.J. Bratton, J. Mater. Sci. 14 (1979) 66–69.
[3] M. Miyayama, H. Yanagida, A. Asada, Am. Ceram. Soc. Bull. 65 (1986) 660–664.
[4] M.J. Verkerk, A.J.A. Winnubst, A.J. Burggraaf, J. Mater. Sci. 17 (1982) 3113–3122.
[5] A.J. Feighery, J.T.S. Irvine, Solid State Ionics 121 (1999) 209–216.
[6] X. Guo, R.Z. Yuan, J. Mater. Sci. 30 (1995) 923–931.
[7] M. Mori, T. Abe, H. Itoh, O. Yamamoto, Y. Takeda, T. Kawahara, J. Am. Ceram. Soc. 77 (1994) 2217–2219.

[8] S. Rajendran, J. Drennan, S.P.S. Badwal, J. Mater. Sci. Lett. 6 (1987) 1431–1434.

[9] A. Rizea, D. Chirlesan, C. Petot, G. Petot-Ervas, Solid State Ionics 146 (2002) 341–353.

[10] A. Yuzaki, A. Kishimoto, Solid State Ionics 116 (1999) 47–51.

[11] E.P. Butler, J. Drennan, J. Am. Ceram. Soc. 65 (1982) 474–478.

[12] S. Tekeli, Compos. Sci. Technol. 65 (2005) 967–972.

[13] F.A. Elrefaie, W.W. Smeltzer, J. Electrochem. Soc. 128 (1981) 2237–2242.

[14] L. Kou, J.R. Selman, J. Appl. Electrochem. 30 (2000) 1433–1437.

[15] I. Halevy, D. Dragoi1, E. Ustundag, A.F. Yue1, E.H. Arredondo, J. Hu, M.S. Somayazulu, J. Phys.-Condens. Mat. 14 (2002) 10511–10516.

[16] E. Ustundag, P. Ret, R. Subramanian, R. Dieckmann, S.L. Sass, Mater. Sci. Eng. A-Struct. 195 (1995) 39–50.

[17] S. Linderoth, N. Bonanos, K.V. Jensen, J.B. Bilde-Sørensen, J. Am. Ceram. Soc. 84 (2001) 2652–2656.

[18] Y.L. Liu, C.G. Jiao, Solid State Ionics 176 (2005) 435–442.

[19] G. de Roos, J.M. Fluit, J.H.W. Dewit, J.W. Geus, Surf. Interface Anal. 3 (1981) 229–234.

[20] S.P.S. Badwal, Solid State Ionics 52 (1992) 23–32.

[21] I.R. Gibson, J.T.S. Irvine, J. Mater. Chem. 6 (1996) 895–898.

[22] S. Amarasinghe, P. Ammala, S. Aruliah, O. Bellon, R. Knibbe, J. Love, R. Ratnaraj, X. Zheng, Solid Oxide Fuel Cells IX (2005) 1037.